

The Cooling Box Problem: Convection with a quadratic equation of state

Jason Olsthoorn[†], Edmund W. Tedford, and Gregory A. Lawrence

Department of Civil Engineering, University of British Columbia, 2002-6250 Applied Science Ln,
Vancouver, BC V6T 1Z4

(Received xx; revised xx; accepted xx)

We investigate the convective cooling of a fluid with a quadratic equation of state by performing three-dimensional direct numerical simulations of a flow with a fixed top-boundary temperature, which is lower than the initial fluid temperature. We consider fluid temperatures near the density maximum, where the nonlinearity is expected to be important. When the equation of state is nonlinear, the resultant vertical transport of heat is fundamentally different and significantly lower than the predictions derived for a linear equation of state. Further, three dimensionless groups parameterize the convective system: the Rayleigh number (Ra_0), the Prandtl number (Pr), and the dimensionless bottom water temperature (T_B). We further define an effective Rayleigh number ($Ra_{eff} = Ra_0 T^2$), which is equivalent to the traditional Rayleigh number used with a linear equation of state. We present a predictive model for the vertical heat flux, the top boundary-layer thickness, and the turbulent kinetic energy of the system. We show that this model agrees well with the direct numerical simulations. This model could be used to understand how quickly freshwater lakes cool in high latitude environments.

1. Introduction

An important feature of freshwater lakes is that they have a nonlinear equation of state (EOS). This nonlinear EOS is nearly quadratic with temperature near the temperature of maximum density, which is above the freezing temperature of the water (e.g. $\tilde{T}_{md} \approx 3.98^\circ\text{C}$ for distilled water at atmospheric pressure). The significance of this nonlinearity for lakes has been recognized for over a century (Whipple 1898). As a result of the density maximum, cooling the surface of a water body that has a mean internal temperature below \tilde{T}_{md} will stabilize the water column resulting in the characteristic reverse temperature stratification found during the winter months in temperate lakes (Farmer 1975). Stratification with temperatures on opposite sides of \tilde{T}_{md} will lead to cabbelling (nonlinear mixing), which has important implications for convection (Farmer and Carmack 1981; Carmack 1979; Couston et al. 2017, 2018). Convection of this type is also relevant in other fields such as Arctic melt ponds (Kim et al. 2018) and geologically sequestered carbon dioxide (Hewitt et al. 2013). This paper aims to understand how thermal convection is altered near \tilde{T}_{md} .

The theoretical studies of such a system date back to Veronis (1963). He considered the linear stability of a fluid layer with fixed temperatures at the top and bottom boundaries; temperatures fixed on either side of \tilde{T}_{md} . Shortly thereafter, Townsend (1964) performed a complementary experimental study, again with fixed temperatures at the top and bottom. Both studies showed that the nonlinear EOS results in a stable upper layer above a convectively unstable lower layer, which will preferentially mix the lower-layer temperature stratification (similar to Figure 1(a)

[†] Email address for correspondence: Jason.Olsthoorn@ubc.ca

except with a bottom thermal boundary layer). Several studies have shown that convection can generate internal waves in the stable upper-layer, which are particularly relevant for astrophysical applications (Bars et al. 2015; Lecoanet et al. 2015). Recently, Toppaladoddi and Wettlaufer (2017) and Wang et al. (2019) built on this previous work and performed two-dimensional and three-dimensional simulations of convection with a nonlinear EOS. Both studies highlighted that in addition to the traditional dimensionless parameters (the Rayleigh number and the Prandtl number) considered for this flow setup, the nonlinear EOS introduces an additional independent parameter. The additional nondimensional parameter quantifies the ratio of the temperature variation across the stable and unstable layers. We will show that a similar ratio is important here. In each of these studies, the top and bottom temperatures are fixed, and the results focus on the statistical steady state.

Most lakes do not reach a steady-state, but warm and cool throughout the year. In addition, the dominant heat loss in these freshwater systems is through the water surface with a relatively insulated bottom. Motivated by these considerations, we study a box of warm fluid ($\tilde{T} > \tilde{T}_{md}$) cooled from above ($\tilde{T} < \tilde{T}_{md}$). Here, unlike the previous studies, the lower boundary is insulating, and the temperature stratification is transient. As is typical of these theoretical studies (Veronis 1963; Townsend 1964; Olsthoorn et al. 2019), we will consider an EOS that is quadratic with temperature, which approximates the full EOS of Chen and Millero (1986) for temperatures below 10 °C. In this paper, we will refer to a cooling of the surface, though the problem is symmetric for a box of cold water that is heated from above, at least for a quadratic EOS assumed here. We want to understand how convection and the resultant heat transport is changed in the presence of this nonlinear density relationship, near \tilde{T}_{md} . In particular, we address the three following questions:

- (i) Does the nonlinear equation of state affect the vertical transport of heat within the water?
- (ii) What parameters determine the heat flux out of the water surface?
- (iii) Can we predict the vertical heat transport and kinetic energy produced by the turbulent convection?

We will begin, in §2, with a discussion of the numerical methods used in this paper. Section §3 is an analysis of the three-dimensional direct numerical simulations, highlighting that the vertical transport of heat is significantly different for a nonlinear EOS than that predicted for a linear EOS. Section 4 discusses the relevant parameters that control the heat flux and present a predictive model for this system. We show that the model agrees well with the data from the numerical simulations in §5. Finally, we conclude in §6.

2. Numerical Setup

We consider a body of water that is insulated from below and cooled from above. We restrict our analysis to freshwater, where the temperature of maximum density \tilde{T}_{md} is above its freezing temperature. Figure 1(b) is a schematic of the numeric domain of interest. We ignore the effects of salinity, pressure, and higher-order terms in the equation of state (EOS) such that the density ($\tilde{\rho}$) is given

$$\tilde{\rho} = \tilde{\rho}_0 - C_T \left(\tilde{T} - \tilde{T}_{md} \right)^2. \quad (2.1)$$

Here, C_T is a constant and $\tilde{\rho}_0$ is the density at $\tilde{T} = \tilde{T}_{md}$.

We are interested in parameterizing the convective heat flux through the top boundary. As such,

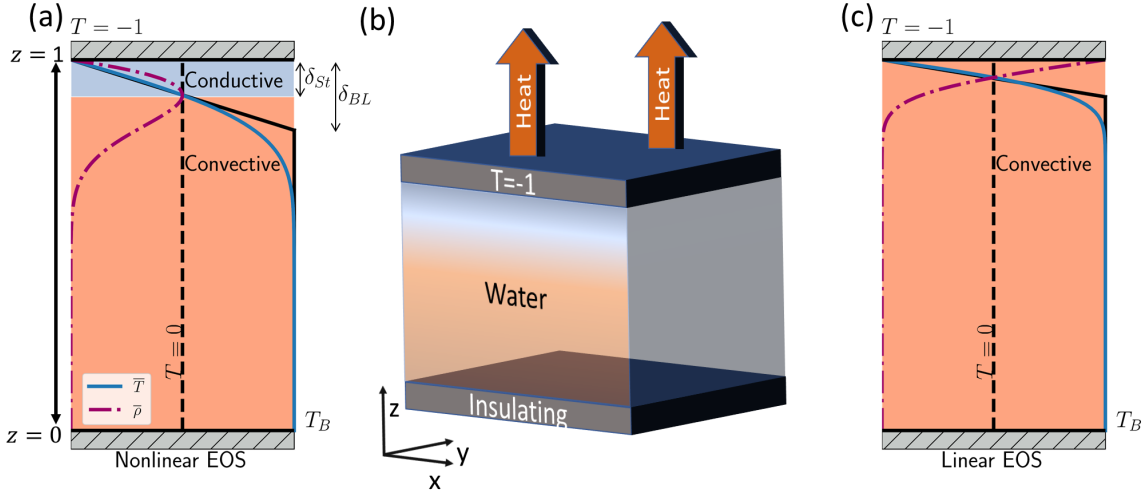


Figure 1: (a) Representative mean temperature (blue line) and density (magenta dashed-dot line) profiles with a nonlinear equation of state. Note the presence of an upper stable thermal boundary-layer (blue). The model's piecewise-linear profiles (equation (4.2)) are also included as a solid black line. (b) A diagram of the numerical domain. (c) Comparative mean temperature and density profiles for a linear equation of state.

a natural time scale for this setup is the diffusive timescale of heat τ_κ over the domain height H . That is,

$$\tau_\kappa = \frac{H^2}{\kappa}, \quad (2.2)$$

where κ is the diffusivity of heat. We then nondimensionalize the spatial coordinates ($\tilde{\mathbf{x}}$), the fluid velocity ($\tilde{\mathbf{u}}$), time (\tilde{t}) and temperature (T) as,

$$\mathbf{x} = \frac{\tilde{\mathbf{x}}}{H}, \quad \mathbf{u} = \frac{\tilde{\mathbf{u}}H}{\kappa}, \quad t = \frac{\tilde{t}}{\tau_\kappa}, \quad T = \frac{\tilde{T} - \tilde{T}_{md}}{\Delta\tilde{T}}. \quad (2.3)$$

Boldface variables denote vector quantities and $\Delta\tilde{T} = \tilde{T}_{md} - \tilde{T}(\tilde{z} = H)$. As an aside, we would like to highlight that, throughout the paper, we have dropped factors of depth $Lz = 1$. While we believe that this is a reasonable simplification, we highlight this convention to avoid any confusion for the reader.

The equations of motion for this flow are the Navier-Stokes equations under the Boussinesq approximation. These equations are written

$$\left(\frac{\partial}{\partial t} + \mathbf{u} \cdot \nabla \right) \mathbf{u} = -\nabla P + \text{Ra}_0 \text{Pr} T^2 \hat{\mathbf{k}} + \text{Pr} \nabla^2 \mathbf{u}, \quad (2.4)$$

$$\left(\frac{\partial}{\partial t} + \mathbf{u} \cdot \nabla \right) T = \nabla^2 T, \quad (2.5)$$

$$\nabla \cdot \mathbf{u} = 0. \quad (2.6)$$

We have defined the Rayleigh number (Ra_0) and Prandtl number (Pr) as

$$\text{Ra}_0 = \frac{g C_T \Delta \tilde{T}^2 H^3}{\rho_0 \kappa \nu}, \quad \text{Pr} = \frac{\nu}{\kappa}, \quad (2.7)$$

where ν is the molecular viscosity of water, and g is the gravitational acceleration. The value of the Prandtl number for freshwater varies from $\text{Pr} \approx 7$ at $\tilde{T} = 20^\circ\text{C}$ to $\text{Pr} \approx 13.4$ at $\tilde{T} = 0^\circ\text{C}$, largely due to variations in ν . Incorporating the functional dependence of ν on T is outside of the scope of this paper. Hay and Papalexandris (2019) performed convective simulations with an evolving Pr , in a different context, that do not show significant changes to the vertical heat flux from the constant Pr case. Future work will discuss the role of the changing viscosity at low temperatures. In this paper, we will assume a constant ν , and prescribe $\text{Pr} = 9$.

We enforce a fixed temperature on the surface and an insulating bottom condition. That is

$$T \Big|_{z=1} = -1, \quad \frac{\partial T}{\partial z} \Big|_{z=0} = 0, \quad (2.8)$$

along with no-slip top and bottom velocity boundary conditions.

As we will see below, the well-mixed bottom-water temperature T_B is an important parameter in this system. As illustrated in Figure 1(a), while the system is convectively unstable, the temperature profile below the top boundary layer is nearly uniform. In the numerical simulations, we will determine T_B by fitting the horizontally averaged temperature profile to an erf function. That is,

$$\bar{T} \approx (1 + T_B) \text{erf} \left(\frac{z-1}{\eta} \right) - 1, \quad (2.9)$$

where $\eta \approx \delta_{BL}$ (defined below) is a fit parameter and $\bar{\cdot} = \frac{1}{L_x L_y} \int \cdot \, dx \, dy$. Over time, T_B will decrease, whereas Ra_0 , by definition, will remain fixed.

In most cases, we selected the initial fluid temperature such that there was an initial symmetry between the bottom water temperature ($T_B = 1$) and the top boundary condition about $T = 0$. For reference, for a water depth of $H = 0.05\text{m}$ with $\tilde{T}(\tilde{z} = H) = 0^\circ\text{C}$, the initial water temperature would be $\tilde{T} \approx 8^\circ\text{C}$ and $\text{Ra}_0 \approx 8 \times 10^5$. Thus, the simulations presented in this paper (see table 1) are on the scale of potential laboratory experiments. In the lowest Ra_0 case, we selected $T_B(t=0) = 2$ so that the initial instability grew significantly quicker than the background diffusion.

While the top boundary temperature will remain fixed ($T(x, y, z = 1, t) = -1$), T_B will cool throughout the numerical simulations. While $T_B > 0$, there exist two sub-domains to the mean temperature stratification: an upper stable stratification of depth δ_{St} where $\bar{T} < 0$ and a lower hydrostatically-unstable stratification where $\bar{T} > 0$. Figure 1(a) is a plot of a representative temperature profile within the fluid domain. The total top boundary-layer thickness between the well-mixed uniform temperature and the upper boundary is $\delta_{BL} > \delta_{St}$ (see Figure 1(a)).

Before continuing, we highlight that for a linear EOS, T_{md} cannot be internal to the fluid domain, and an upper stable layer cannot form. As such, for a linear EOS, we would expect a temperature profile to resemble that in Figure 1(c).

2.1. Numerical Implementation

We performed direct numerical simulations using SPINS (Subich et al. 2013). SPINS solves the Navier-Stokes equations under the Boussinesq approximation using pseudospectral spatial derivatives and a third-order time-stepping scheme. As the top boundary-layer controls the dynamics

Case	EOS	Domain Size (Lx × Ly × Lz)	Resolution (Nx × Ny × Nz)	Ra ₀	Pr	T _B (t = 0)	max $\frac{\Delta x}{\eta_B}$
1	Quadratic	4 × 4 × 1	256 × 256 × 128	9.0 × 10 ⁴	9	2	1.5
2	Quadratic	4 × 4 × 1	256 × 256 × 256	4.5 × 10 ⁵	9	1	1.8
3	Quadratic	4 × 4 × 1	256 × 256 × 256	9.0 × 10 ⁵	9	1	2.1
4	Quadratic	4 × 4 × 1	512 × 512 × 256	4.5 × 10 ⁶	9	1	1.6
5	Quadratic	4 × 4 × 1	512 × 512 × 256	9.0 × 10 ⁶	9	1	2.2
6	Linear	4 × 4 × 1	256 × 256 × 256	9.0 × 10 ⁵	9	1	1.9

Table 1: Table of the parameters for each numerical simulation.

of the initial instability and the subsequent convection, we implement a Chebyshev grid in the vertical, which clusters grid points at the domain boundaries. We assume periodic horizontal boundary conditions, implemented with Fast Fourier Transforms.

We performed five numerical simulations with a nonlinear EOS at different Rayleigh numbers. We performed one additional simulation with a linear EOS for comparison. The details of these numerical simulations are provided in Table 1. In all six cases, the Rayleigh number was large enough for the system to become unstable (See Appendix C for the linear stability analysis). We initially perturb the three velocity components with a random perturbation sampled from a Normal distribution scaled by 10^{-2} . The numerical resolution (Nx × Ny × Nz) was selected, such that $\max \frac{\Delta x}{\eta_B} < 3$, where we compute the Batchelor scale $\eta_B = (\bar{\varepsilon})^{-\frac{1}{4}} \text{Pr}^{-\frac{1}{2}}$, for viscous dissipation rate ε (see equation (4.7)) and horizontal grid spacing Δx . The vertical grid is clustered towards the boundaries and $\max \frac{\Delta z}{\eta_B} < \max \frac{\Delta x}{\eta_B}$, in all cases. This resolution criterion is similar to that employed in Hay and Papalexandris (2019); Kaminski and Smyth (2019); Olsthoorn et al. (2019); Smyth and Moum (2000). The resolution sufficiency is highlighted in Appendix D.

3. Simulation Results

In this section, we describe both the qualitative and quantitative dynamics of the numerical simulations as they relate to the transport of heat within the fluid domain. In particular, we show that the convection is self-similar in T_B for the range of Rayleigh numbers considered. Our discussion is focused on a single representative case: Case 3, Ra = 9.0 × 10⁵. The results are similar for the other simulations, except where otherwise noted.

Figure 2 contains snapshots of the temperature field for Case 3. The left column of Figure 2 contains plots of the temperature field at different times $t = \{2.50 \times 10^{-3}, 5.00 \times 10^{-3}, 7.50 \times 10^{-3}, 1.00 \times 10^{-2}, 1.25 \times 10^{-2}, 5.00 \times 10^{-2}\}$. These plots were made with VisIt’s (Childs et al. 2012) volume plot option that varies the transparency of the temperature field according to its value. The downwelling plumes are visible in the $X - Z$ slices (Figure 2 (middle)). Initially, the temperature stratification is linearly stable, and the temperature profile simply diffuses. At $t = 0.0025$ (Figure 2(a)-(c)), the temperature stratification matches that predicted by pure diffusion. Once the top thermal boundary-layer has grown sufficiently, the system is unstable, and small perturbations to the velocity and temperature field will grow. These near-modal perturbations are visible at $t = 5.00 \times 10^{-3}$ (Figure 2(d)-(f)). Once the perturbations grow large enough, they begin to merge, forming dense plumes that transport cold fluid to the bottom of the domain. The columnar plumes are highly variable in both space and time, and the resultant convection will mix the bottom

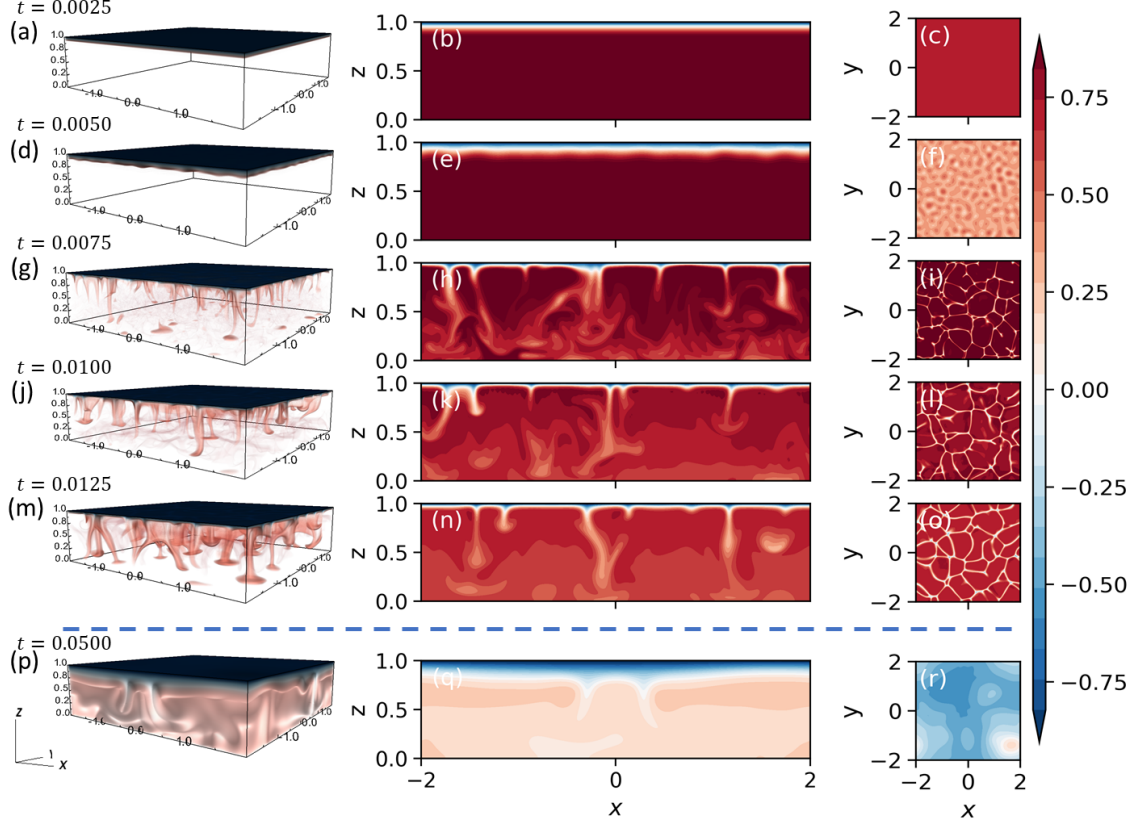


Figure 2: Snapshots of the temperature field for Case 3: $Ra_0 = 9.0 \times 10^5$, $Pr = 9$. The volume plots $\{(a),(d),(g),(j),(m),(p)\}$ encapsulate the three-dimensional structure of the flow field. The middle figure panels $\{(b),(e),(h),(k),(n),(q)\}$ are contour plots of vertical ($x - z$) temperature slices at $y = -1$. Similarly, The right figure panels $\{(c),(f),(i),(l),(o),(r)\}$ are contour plots of horizontal ($x - y$) temperature slices at $z = 0.9$. Snapshots are given at $t = 2.50 \times 10^{-3}$ (a)-(c), $t = 5.00 \times 10^{-3}$ (d)-(f), $t = 7.50 \times 10^{-3}$ (g)-(i), $t = 1.00 \times 10^{-2}$ (j)-(l), $t = 1.25 \times 10^{-2}$ (m)-(o), and $t = 5.00 \times 10^{-2}$ (p)-(r). Note the jump in output times highlighted by the horizontal dashed line.

fluid. Eventually (Figure 2(p)-(r)), the bottom water temperature reduces sufficiently such that the vertical heat flux rapidly decreases.

Slices of the spanwise ($X - Y$) structure of the temperature field at $z = 0.9$ are presented in Figure 2 (right). While a complete analysis of this structure is outside of the scope of this paper, we highlight it here as it demonstrates that the spacing between the downwelling plumes is increasing over time. The horizontal length scale of the three-dimensional flow structure increases as $T_B \rightarrow 0$, as viscous dissipation preferentially diffuses small scale motions. Eventually, the spacing between the plumes reaches the size of the domain, which limits the run time of these simulations. We have

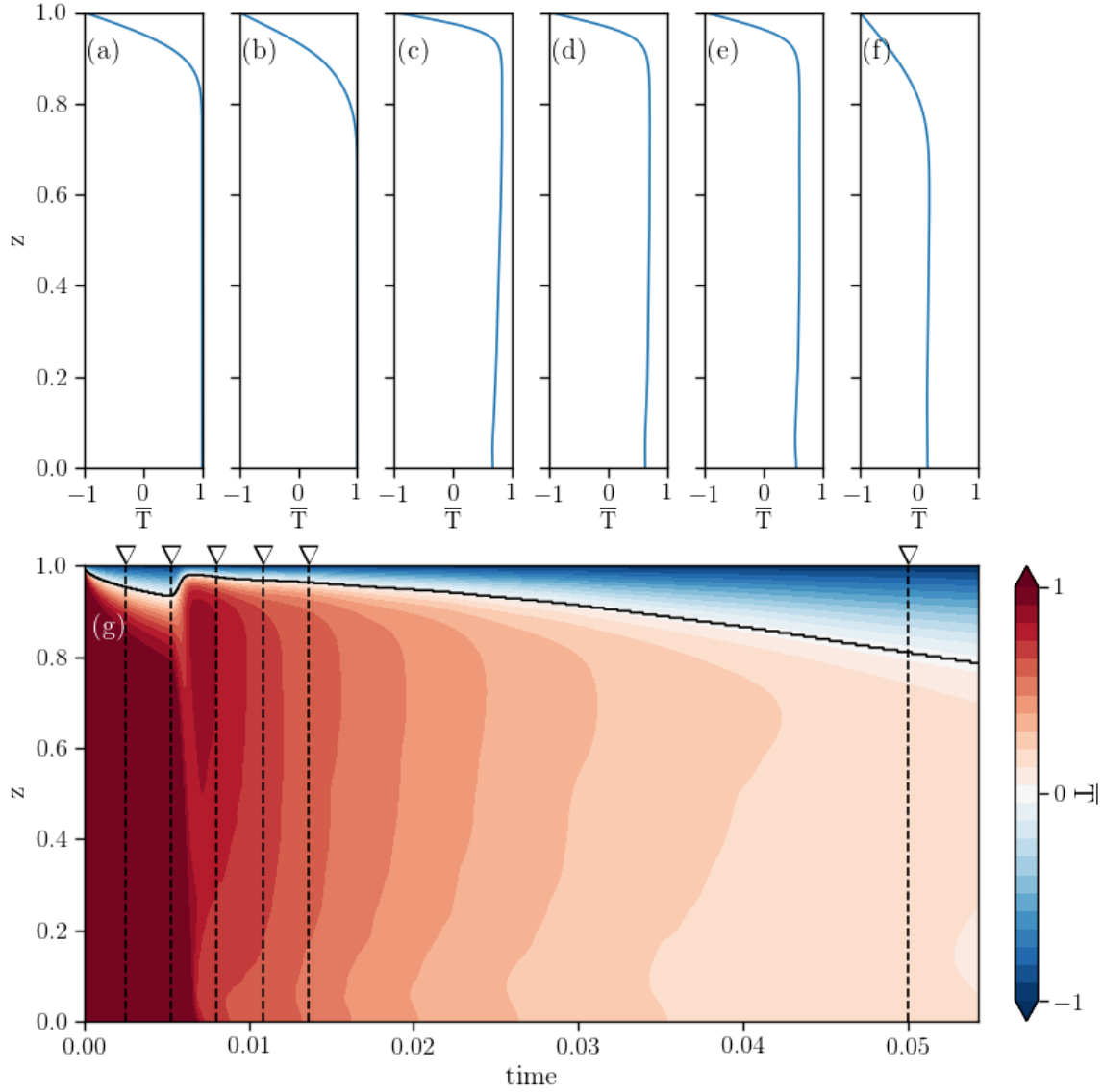


Figure 3: The horizontally averaged temperature profiles are plot at the output time of the snapshots of Figure 2 ($t = 2.50 \times 10^{-3}$ (a), $t = 5.00 \times 10^{-3}$ (b), $t = 7.50 \times 10^{-3}$ (c), $t = 1.00 \times 10^{-2}$ (d), $t = 1.25 \times 10^{-2}$ (e), and $t = 5.00 \times 10^{-2}$ (f)). Contours of the horizontally averaged temperature (\bar{T}) over time are also plotted (g). The vertical dashed lines in panel (g) represent the time of the vertical temperature profiles. Data is shown for Case 3: $Ra_0 = 9.0 \times 10^5$.

performed several simulations at different domain sizes and have determined that the present results are not domain size-dependent.

We highlight the mean structure of the temperature stratification in figure 3(a)-(f), which are

plots of individual horizontally-averaged temperature profiles at times $t = \{2.50 \times 10^{-3}, 5.00 \times 10^{-3}, 7.50 \times 10^{-3}, 1.00 \times 10^{-2}, 1.25 \times 10^{-2}, 5.00 \times 10^{-2}\}$ (identical to Figure 2). The evolution of the temperature stratification is further highlighted in the contours of horizontally-averaged temperature over time (Figure 3(g)). These contours show that the boundary-layer depth increases over time and that the bottom water temperature decreases. Note that there is a weak thermal gradient near the bottom of the domain due to the solid boundary. This thermal gradient becomes weaker with increasing Ra, due to the increased energy within the system.

3.1. Vertical Heat Transport

Now that we have presented the essential features of the temperature evolution, we proceed to quantify the heat loss resulting from the thermal convection. The rate of heat loss of the water in the domain is

$$\frac{d}{dt} \int_0^1 \int_A T \, dA \, dz = -FA, \quad (3.1)$$

where F is the average outward heat flux at the domain surface, and $A = L_x L_y$ is the area of the water surface. The vertical transport of heat is approximately constant over the upper conductive boundary-layer.

The vertical heat flux within the convective layer is significantly greater than the diffusive flux. We define σ as the ratio of average heat flux to the diffusive heat flux over the convective domain. That is, we write

$$\sigma \approx \frac{F / (1 - \delta_{St})}{(T_U - T_0) / (1 - \delta_{St})} = \frac{F}{T_U - T_0}, \quad (3.2)$$

where T_0 is the temperature of maximum density within the domain. As we will see below, for a quadratic EOS, σ is constant for a significant portion of the simulation time, which indicates the temperature decays exponentially. For a linear EOS, T_0 will be equal to the top-boundary temperature ($T_0 = -1$). In this case, σ is identical to the Nusselt number (Nu), which is the ratio of the average vertical heat flux to the diffusive heat flux across the entire domain. For the nonlinear EOS discussed here, where the temperature of maximum density is interior to the fluid domain, then $T_0 = 0$.

As an aside, it is worth noting that F itself is a function of the temperature difference $T_U - T_0$. As the water becomes uniform, $(T_U - T_0) \rightarrow 0$, the vertical flux $F \rightarrow 0$ such that σ is bounded.

As a simple model, we first consider the scenario where the water column is uniformly mixed to some temperature T_U . If σ were a constant σ_0 , then

$$\frac{d}{dt} T_U A = -\sigma_0 \cdot (T_U - T_0) A \implies T_U = B \exp(-\sigma_0 t) + T_0, \quad (3.3)$$

where B is a constant of integration. That is, T_U decays exponentially in time. In principle, there is no *a priori* reason to suspect that σ will be constant and, in general, it is not. However, as we will show below, for the initial convective evolution, σ is constant, and the temperature will decay exponentially.

Before continuing, we return to the first of the main questions we are trying to answer in this paper. Does the nonlinear equation of state affect the vertical transport of heat out of the domain? We performed a single numerical simulation with a linear EOS with $Ra_0 = 9.0 \times 10^5$ and $Pr = 9$. The boundary and initial conditions remain unchanged. For a linear EOS, there are only two free

parameters: a Prandtl number (Pr) and a time-dependent Rayleigh number. The relevant Rayleigh number for a linear EOS includes the density difference across the domain $\Delta\rho$ as

$$\text{Ra}_{Lin} = \frac{g\Delta\rho H^3}{\rho_0 \kappa\nu} = \text{Ra}_0 (1 + T_B). \quad (3.4)$$

Here, we have related the constant Rayleigh number (Ra_0) defined in this paper with a more traditionally defined time-varying Rayleigh number (Ra_{Lin}), used with a linear EOS. The equivalent effective Reyleigh number (Ra_{eff}) for the quadratic EOS is given:

$$\text{Ra}_{eff} = \text{Ra}_0 T_B^2. \quad (3.5)$$

We will return to this in our discussion of σ below.

For a linear equation of state, it is empirically determined that

$$\text{Nu}_{Lin} \propto \text{Ra}_{Lin}^n. \quad (3.6)$$

While significant controversy persists over the exact value of n (for example, see Plumley and Julien 2019)), we will specify $n = 0.28$ as it best fits the data discussed below.

Figure 4 is a comparison plot of the (a) temperature and (b) vertical heat flux as a function of time, a comparison between a linear or a quadratic EOS. The scaling (3.6) is included in panel (b). Here, and for the rest of the paper, we plot in grey the initial transition period before reaching a quasi-equilibrium (where the vertical buoyancy flux approximately balances viscous dissipation). We observe that the curvature in the EOS fundamentally changes the temperature evolution of the system over time. The surface heat flux is significantly greater for the linear EOS, resulting in the bottom water temperature T_B decaying much faster for a linear EOS. For the quadratic EOS, the presence of a temperature of maximum density also restricts the convective mixing such that $T_B \rightarrow 0$ (note that molecular diffusion will eventually reduce $T_B \rightarrow -1$ as $t \rightarrow \infty$). If we return to the dimensional example of a 0.05 m deep container with a surface temperature at 0 °C, then by $t = 0.05$ (≈ 15 minutes) there is a 1.5 °C degree difference between the internal temperatures of the linear and quadratic EOS; nearly a 40% increase in the heat loss!

The Nusselt number dependency in equation (3.6) is inadequate to describe the temperature evolution for a quadratic EOS. In the next section, we derive a model for the vertical heat flux (F) and turbulent kinetic energy density (TKE) of convection with a nonlinear EOS. We will show that the convection is fundamentally dependent on three independent parameters, as opposed to the two needed with a linear EOS.

4. Scaling Laws

We begin with a Reynolds decomposition of the temperature and velocity field into a mean temperature profile and fluctuations from it, where

$$\mathbf{u} = \mathbf{0} + \mathbf{u}', \quad T = \bar{T} + T'. \quad (4.1)$$

In the numerical simulations, we will take $(\bar{\cdot})$, the horizontal average through the domain. For this scaling analysis, we will simplify \bar{T} as a piecewise linear profile

$$\bar{T} = \begin{cases} -1 - \frac{1+T_B}{\delta_{BL}} (z - 1) & z > 1 - \delta_{BL}, \\ T_B & z \leq 1 - \delta_{BL}, \end{cases} \quad (4.2)$$

as in Figure 1(a). Note that δ_{BL} is the total transition thickness with $\delta_{BL} > \delta_{St}$.

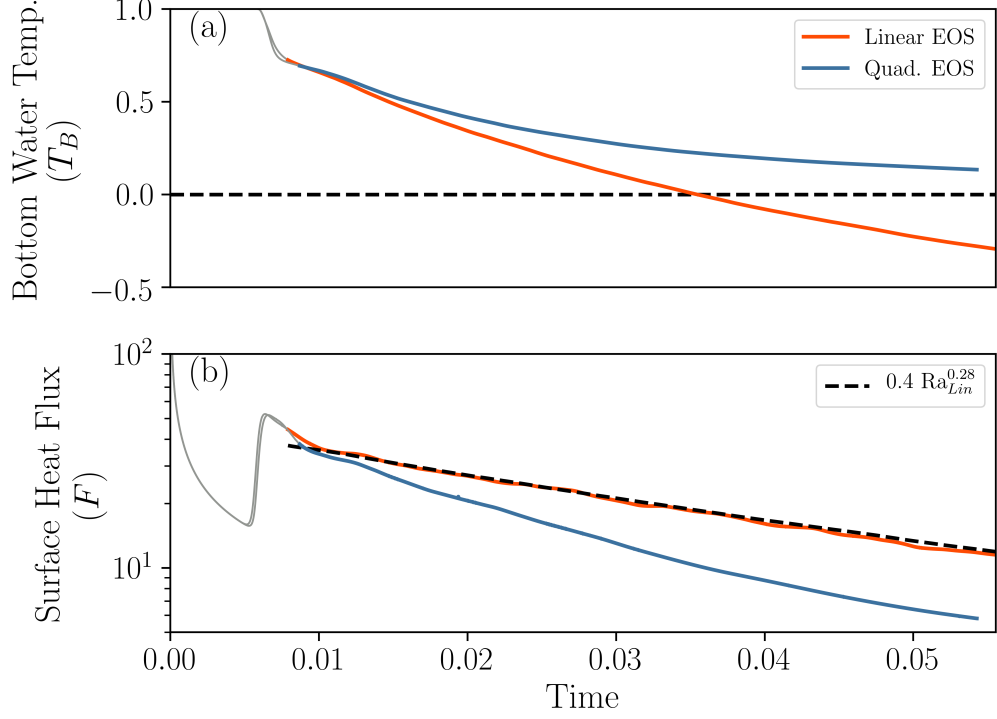


Figure 4: A comparison plot of (a) T_B and (b) F versus time between convection with a linear or a quadratic equation of state. The temperature of maximum density is included as a horizontal dashed line in (a). The scaling (3.6) is included as a dashed line in panel (b). In both cases, $\text{Ra}_0 = 9.0 \times 10^5$. We plot in grey the initial (diffusive) transition period.

4.1. Boundary-Layer Thickness δ_{St}

The diffusion of heat through the top boundary is

$$F = -\left. \frac{\partial \bar{T}}{\partial z} \right|_{z=1} = \frac{1 + T_B}{\delta_{BL}} = \frac{1}{\delta_{St}}.$$

That is, in this nondimensionalization, the boundary layer thickness solely determines the outward heat flux. As a reminder, δ_{St} is the top stable boundary-layer thickness between the top boundary and where $\bar{T} = 0$ (the temperature of maximum density).

Substituting the Reynolds decomposition (4.1) into the temperature evolution equation (2.5), we derive the evolution equation for the mean temperature profile,

$$\frac{\partial \bar{T}}{\partial t} = -\frac{\partial}{\partial z} \left(-\frac{\partial \bar{T}}{\partial z} + \overline{T'w'} \right). \quad (4.3)$$

Balancing the heat fluxes within the domain and top boundary layer, we determine

$$-\underbrace{\frac{\partial T_B}{\partial t} (1 - (1 + T_B) \delta_{St})}_{\text{Interior Cooling}} + \underbrace{\frac{(1 + T_B)^2}{2} \frac{\partial \delta_{St}}{\partial t}}_{\text{Increased } \delta_{St}} = \underbrace{\frac{1}{\delta_{St}}}_{\text{Outward Heat Flux}}. \quad (4.4)$$

Appendix A provides a derivation of (4.4). We can see from equation (4.4) that a fraction of the heat loss is derived from the cooling of the interior fluid. The remainder of the heat loss is given by an increase in the boundary layer thickness δ_{St} . The surface heat loss is controlled by the boundary layer thickness δ_{St} .

Building on §3.1, the average temperature within the domain is T_B such that,

$$\frac{dT_B}{dt} = -\sigma T_B. \quad (4.5)$$

As convection greatly enhances the vertical flux of temperature, we find that $\sigma \gg 1$. We will continue a discussion of σ below. To leading order in $O(\frac{1}{\sigma})$, the dominant balance between the interior cooling and the outward heat flux determines that

$$\delta_{St} \sim \frac{1}{\sigma T_B}, \quad F = \frac{1}{\delta_{St}} \sim \sigma T_B, \quad \sigma \gg 1. \quad (4.6)$$

4.2. Turbulent Kinetic Energy

Similar to equation (4.3), the volume integrated turbulent kinetic energy density (TKE = $\frac{1}{2} \mathbf{u}' \cdot \mathbf{u}'$) evolution equation is written

$$\frac{d \langle \text{TKE} \rangle_V}{dt} = -\text{Ra}_0 \text{Pr} \langle w' \rho' \rangle_V - \varepsilon, \quad \varepsilon = \text{Pr} \langle \nabla \mathbf{u}' : \nabla \mathbf{u}' \rangle_V. \quad (4.7)$$

The $(:)$ operator is the double dot product. Unlike the case of a linear EOS, the vertical buoyancy flux ($w' \rho'$) is not directly proportional to the vertical temperature flux ($w' T'$). For a quadratic EOS, the vertical buoyancy flux is the sum of two components,

$$\overline{w' \rho'} = -2 \overline{w' T' T'} - \overline{w' T' T'}. \quad (4.8)$$

Along with the mixing coefficient (Γ , the ratio of the vertical buoyancy flux to viscous dissipation), we define a buoyancy flux ratio (λ) to quantify the relative contribution of each buoyancy flux term. These are defined as

$$\Gamma = \frac{-\text{Ra}_0 \text{Pr} \langle \overline{w' \rho'} \rangle_V}{\varepsilon}, \quad \lambda = \frac{-\langle \overline{w' T' T'} \rangle_V}{\langle \overline{2w' T' T'} \rangle_V}. \quad (4.9)$$

Assuming self-similarity of TKE, we can show that (see Appendix B for details)

$$\langle \text{TKE} \rangle_V \sim \frac{1}{2} (\Gamma^{-1} - 1) (1 - \Lambda) \text{Ra}_0 \text{Pr} T_B^2, \quad \sigma \gg 1, \quad (4.10)$$

where Γ is assumed constant and

$$\Lambda = \frac{2}{T_B^2} \int_{T_B} T' \lambda(T') dT'. \quad (4.11)$$

This model for the kinetic energy is consistent with the empirical Reynolds number scaling found in Wang et al. (2019).

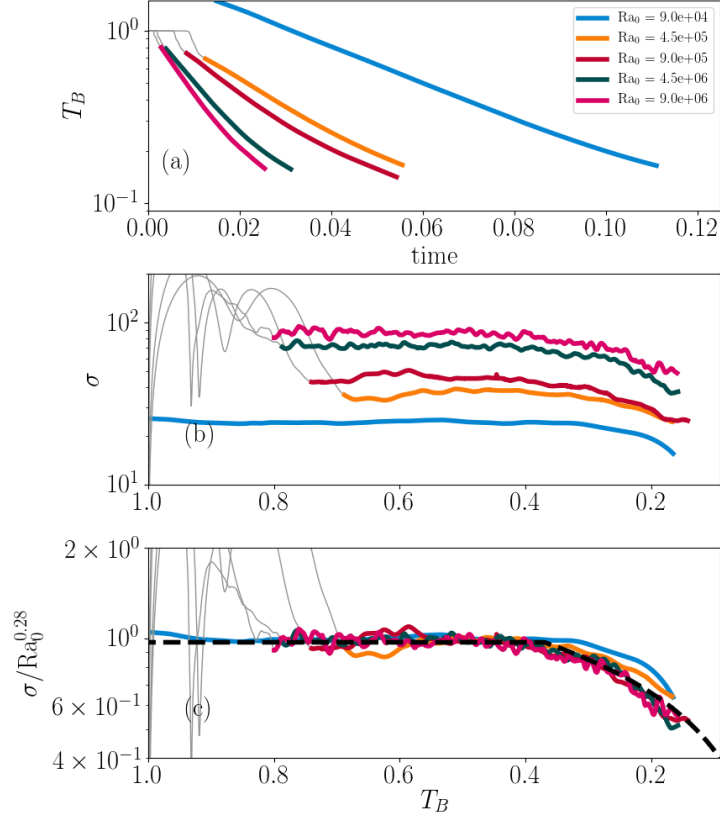


Figure 5: Panel (a) is a plot of the bottom water temperature T_B with time for all numerical runs with a nonlinear EOS. Panel (b) is a plot of the instantaneous decay rate (σ) as a function of T_B . Panel (c) is a plot of the scaled decay rates (σ), which collapse onto a single curve. We include the scaling (5.1) as a dotted black line in panel (c). We plot in grey the initial transition period before reaching a quasi-equilibrium state. Note that the x-axis has been reversed in panels (b),(c), with T_B decreasing towards the right such that it reads in the same direction as time.

What parameters control the heat flux out of the water surface? The scaling laws (4.6) and (4.10) depend on three undetermined coefficients: the decay rate σ , the buoyancy flux ratio λ , and the mixing coefficient Γ . These three coefficients are, as we will show, functions of the three parameters Ra_0 , Pr and T_B . In the next section, we will derive the functional form of σ , λ , and Γ , and show that the models provided here agree well with the simulated quantities.

5. Model Comparison

As discussed above, T_B initially decays exponentially with time. Figure 5(a) is a plot of T_B as a function of time on a semi-log axis for all five of the nonlinear EOS simulations listed in Table 1.

We compute the instantaneous decay rate as

$$\sigma = \frac{-1}{T_B} \frac{dT_B}{dt},$$

and we observe (Figure 5(b)) that, after an initial transient, σ is nearly constant over a range of T_B , with $\sigma \gg 1$ ($T_B \gtrsim 0.37$). During this period, we perform a linear regression to determine the Ra_0 -number dependence of the flow. Figure 5(c) is a plot of σ , scaled by $\text{Ra}_0^{0.28}$, which collapses the data for all of the simulations with a nonlinear EOS. For lower values of T_B ($T_B \lesssim 0.37$), σ decreases with T_B . Once the system has achieved a quasi-steady state, we fit piecewise-curves to the different cases and approximate

$$\sigma = 0.97\text{Ra}_0^{0.28} \begin{cases} 1, & T_B \geq 0.37 \\ \left(\frac{T_B}{0.37}\right)^{0.63}, & T_B < 0.37 \end{cases}. \quad (5.1)$$

We find a regime change at $T_B \approx 0.37$, between a constant exponential decay ($T_B \gtrsim 0.37$), and when σ rapidly decreases ($T_B \lesssim 0.37$). We note that the model presented in §4 is applicable only for $\sigma \gg 1$. As $T_B \rightarrow 0$, σ decreases and higher-order corrections are increasingly significant. It is also worth noting that Case 1: $\text{Ra}_0 = 9.0 \times 10^4$ has the lowest value of σ and Ra_0 , and does not collapse as well as the other cases.

In connection with the linear EOS, we might expect that σ should scale with an effective Rayleigh number (Ra_{eff}) (as was highlighted in Anders et al. (2020)). This is partially correct. To justify this statement, we approximate equation (5.1) as:

$$\frac{\sigma}{\sigma_0} \approx \min \{ \text{Ra}_{max}^{0.28}, \text{Ra}_{eff}^{0.28} \}, \quad \text{Ra}_{max} = \text{Ra}_{eff}(T_B = T_{max}), \quad (5.2)$$

where $\sigma_0 = 0.97T_{max}^{-0.63}$, and $T_{max} = 0.37$. That is, the temperature decay rate σ does increase with Ra_{eff} below some threshold value. For large enough Ra_{eff} , the convection is sufficiently turbulent that σ remains constant. Thus, the convection is self-limiting. We believe this results from the increased diffusion at the top boundary due to the stable thermal layer that is not present in a linear equation of state. Importantly, as highlighted in Toppaladoddi and Wettlaufer (2017); Wang et al. (2019), a third parameter must be defined to characterize the convection. We define that third parameter as T_B .

The mixing coefficient Γ and buoyancy flux ratio λ , defined in equations (4.9), are also functions of the nondimensional parameters. Figure 6 is a plot of (a) λ and (b) Γ as a function of T_B . We find that λ increases as T_B decreases. Fitting λ as a function of T_B with a piecewise-functions, we estimate that while in quasi-steady state,

$$\lambda = 0.24 \begin{cases} T_B^{-\frac{1}{2}}, & T_B \geq 0.35 \\ 1, & T_B < 0.35 \end{cases}. \quad (5.3)$$

As the data is noisy, our estimated power-law dependencies are rough approximations, preferentially weighting the fit values of the higher Ra_0 cases. We anticipate future work to illuminate a theoretical prediction for the appropriate scaling laws. In addition, it is important to note that Case 1: $\text{Ra}_0 = 9.0 \times 10^4$ does not follow the trend of the other cases. For Case 1, the low Rayleigh number results in a significant diffusive contribution to the total heat flux and is in a weakly unstable regime. As in equation (5.1), we find that there is a regime change that occurs at $T_B \approx 0.37$. Similarly, we find that

$$\Gamma \approx 0.96$$

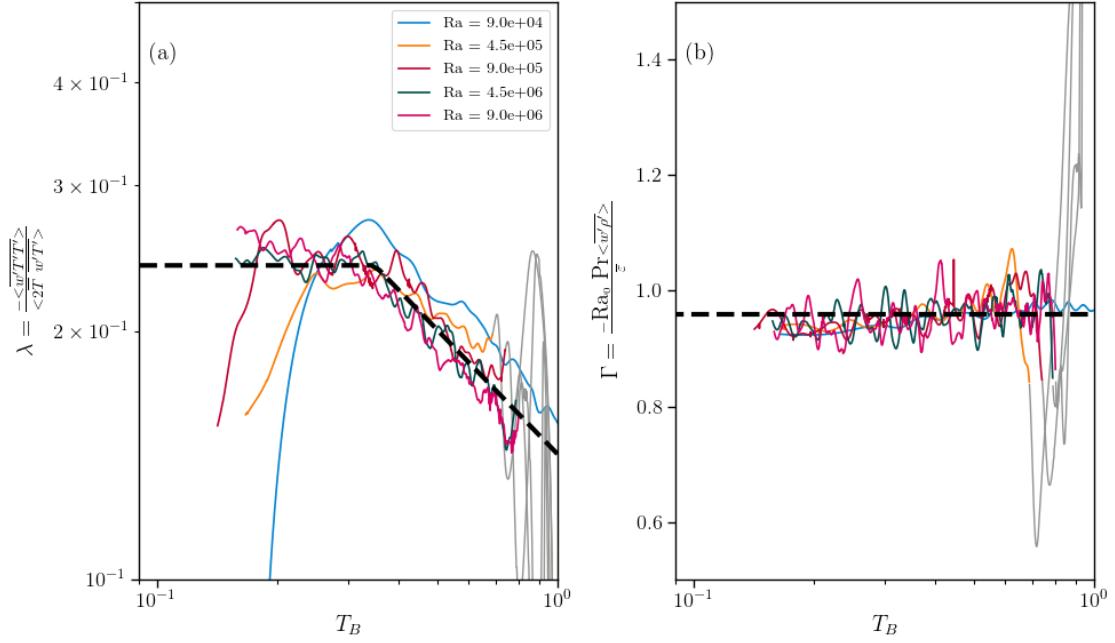


Figure 6: Plot of (a) the buoyancy flux ratio λ and (b) the mixing coefficient Γ as a function of T_B . We include the fit of equation (5.3) as a dashed line in panel (a). We further include a dashed line at $\Gamma = 0.96$ in panel (d). We plot in grey the initial transition period before reaching a quasi-equilibrium state.

for all Ra_0 , though large fluctuations are present. This value of Γ indicates that the rate of viscous dissipation is nearly equal to the vertical buoyancy flux. In steady-state, by definition, $\Gamma = 1$ which is consistent with our observation that that the cooling box is nearly in steady state.

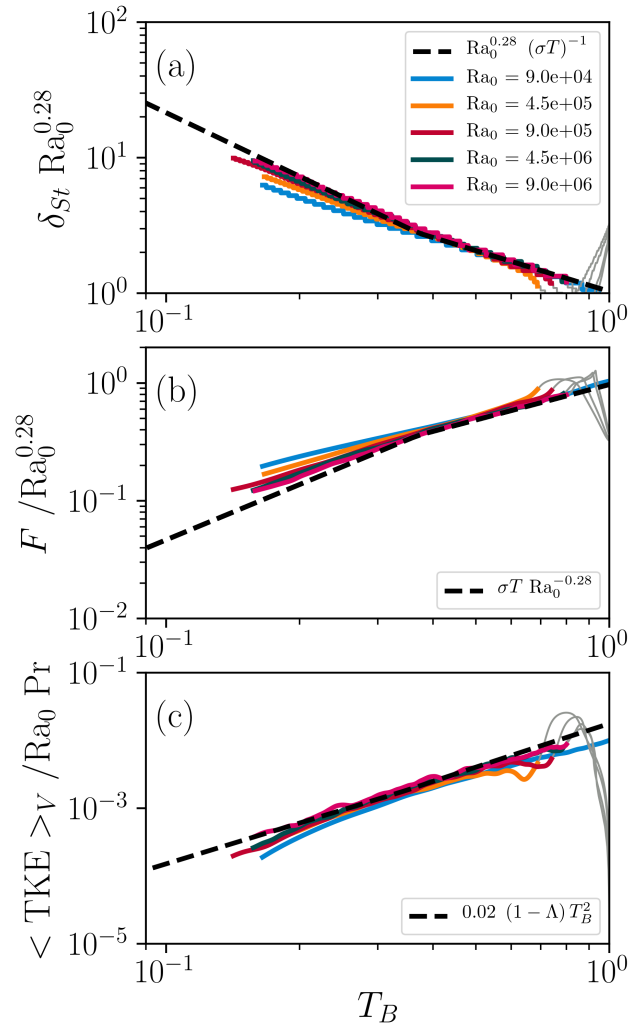


Figure 7: A plot of the scaled (a) boundary layer thickness δ_{st} , (b) surface heat flux F , and (c) turbulent kinetic energy density TKE, as a function of T_B . The black dashed lines denote the predictions of (4.6) and (4.10).

5.1. Model Agreement

Can we predict the vertical heat transport and kinetic energy produced by the turbulent convection? In §4, we derived scaling laws for δ_{st} , F , and TKE as a function of Ra_0 , Pr , and T_B . Figure 7 is a comparison plot between the model equations (4.6) and (4.10) and the numerically computed (a) δ_{st} , (b) F , and (c) TKE. The model agrees well with the data from the direct numerical simulations. We have scaled the y-axes by the appropriate powers of Ra_0 and Pr . Note that the

scaling coefficient 0.02 in panel (c) is equivalent to $\Gamma = 0.96$. The parameters σ and Λ are defined using the fit equations (5.1) and (5.3), respectively.

We further find that as the bottom water $T_B \rightarrow 0$, the simulated values of δ and F appear to diverge from the model. We recall the model equations (4.6) are valid for $\sigma \gg 1$. As the decay rate σ increases with Ra_0 , the larger values of Ra_0 show better agreement between the model and the simulated data. Similarly, Case 4 - $\text{Ra}_0 = 9 \times 10^4$ exhibits the largest deviation from the model fit as it also is the lowest Ra_0 simulation. As the bottom water temperature decreases ($T_B \rightarrow 0$), σ decreases rapidly. The first-order approximation (equation (4.6)) is not expected to perform well in that limit. Higher-order corrections can account for this discrepancy, but that is outside of the scope of this article.

The flow transition that occurs at $T_B \approx 0.37$ (see equations (5.1) and (5.3)) results in a ‘kink’ in the modelled predictions, as seen in Figure 7. We do not yet have a prediction for this limiting temperature value of $T_{max} = 0.37$. However, this transition is important in the evolution of δ_{St} , F and, to a lesser extent, TKE.

6. Conclusions

We considered a box of warm fluid, cooled from the surface through a fixed-temperature boundary condition. In this box, the density was quadratic with temperature. The top boundary temperature and the initial domain temperature were selected to be on opposite sides of the temperature of maximum density, leading to the generation of convection and the formation of an upper stable layer and a lower convectively unstable layer. As the convection mixed the lower-layer fluid, its near homogeneous temperature decreased ($T_B \rightarrow 0$).

We developed a model for our system and scaling laws for δ_{St} , F , and TKE,

$$\delta_{St} \sim \frac{1}{\sigma T_B}, \quad F = \frac{1}{\delta_{St}} \sim \sigma T_B, \quad \sigma \gg 1 \quad (6.1)$$

$$\langle \text{TKE} \rangle_V \sim \frac{1}{2} (\Gamma^{-1} - 1) (1 - \Lambda) \text{Ra}_0 \text{Pr} T_B^2. \quad (6.2)$$

Analyzing the numerical simulations, we determined the Ra_0 and T_B dependence of the decay σ and the integrated buoyancy flux ratio Λ . We showed that the mixing coefficient Γ was effectively constant over the whole range of parameters considered here. Once determined, the model equations agreed well with the numerically computed δ_{St} , F , and TKE.

This paper’s main goal was to understand how convection is changed when the equation of state is nonlinear. We have shown that :

- (i) The surface heat flux is dramatically different, in both magnitude and parameter dependence, between a nonlinear and linear equation of state.
- (ii) In addition to the Rayleigh and Prandtl number, convection with a quadratic equation of state depends on a third nondimensional parameter, the bottom water temperature T_B .
- (iii) Our model (6.1)-(6.2) accurately predicts the heat flux (F), boundary layer thickness (δ_{St}), and turbulent kinetic energy (TKE) based on these three parameters.

This work is a crucial step towards understanding how a nonlinear equation of state modifies convection. The quadratic equation of state limits the vertical heat flux and the kinetic energy,

compared to a linear equation of state, and depends on an additional nondimensional parameter T_B . We are in the process of constructing a Cold Convection Facility, capable of convectively cooling the surface of a fresh body of water to run complementary laboratory experiments. This work provides a framework, including the essential parameters and model considerations, to understand that much more complicated system and, subsequently, freshwater systems in the environment.

Declaration of Interests: The authors report no conflict of interest.

Acknowledgements

We want to thank Andrew Wells, Hugo Ulloa, and Louis-Alexandre Couston for their feedback on this work. This work was funded in part by the Natural Sciences and Engineering Research Council of Canada, the Isaak Killam Trust, and Syncrude Canada Ltd.

Appendix A. Derivation of the scaling law for δ_{St}

First, assuming a piecewise-linear profile for \bar{T} , we can establish that

$$\delta_{BL} = (1 + T_B) \delta_{St}. \quad (\text{A } 1)$$

The rate of change of the total temperature within the domain is then,

$$\frac{d}{dt} \int_0^1 \bar{T} dz = \frac{d}{dt} \left(\int_0^{1-\delta_{BL}} T_B dz + \int_{1-\delta_{BL}}^1 \left(-1 - \frac{1}{\delta_{St}} (z-1) \right) dz \right) \quad (\text{A } 2)$$

$$= \frac{dT_B}{dt} (1 - \delta_{BL}) - \frac{1}{2} \frac{\delta_{BL}^2}{\delta_{St}^2} \frac{\partial \delta_{St}}{\partial t} \quad (\text{A } 3)$$

Noting that the top temperature gradient prescribes the rate of change of heat within the domain, and including (A 1), we arrive at

$$\frac{dT_B}{dt} (1 - (1 + T_B) \delta_{St}) - \frac{(1 + T_B)^2}{2} \frac{\partial \delta_{St}}{\partial t} = -\frac{1}{\delta_{St}} \quad (\text{A } 4)$$

If we further evaluate

$$\frac{dT_B}{dt} \sim -\sigma T_B, \quad \delta_{St} \ll 1, \quad \sigma \gg 1,$$

then to leading order

$$\delta_{St} \sim \frac{1}{\sigma T_B}, \quad \sigma \gg 1. \quad (\text{A } 5)$$

Appendix B. Derivation of the scaling law for TKE

We first recall the Reynolds decomposition

$$\mathbf{u} = \mathbf{0} + \mathbf{u}', \quad T = \bar{T} + T'.$$

The density flux is then written out as

$$\rho = -T^2 = -\left(\bar{T}^2 + 2\bar{T}T' + T'T' \right) \implies \overline{w'\rho'} = -2\overline{w'T'} \bar{T} - \overline{w'T'T'}.$$

For $z < 1 - \delta_{BL}$, the temperature stratification is well mixed, and thus

$$\overline{T'w'} = -\frac{dT_B}{dt}z = \sigma T_B z, \quad z < 1 - \delta_{BL} \implies \langle 2\overline{w'T'} \bar{T} \rangle_V \approx \int_0^1 2\sigma T_B^2 z \, dz = \sigma T_B^2, \quad \delta_{BL} \ll 1.$$

The approximations can be formalized by performing the full integrals and expanding the δ_{BL} as a perturbation series in $\frac{1}{\sigma}$. Therefore, the TKE equation reduces to

$$\frac{d \langle \text{TKE} \rangle_V}{dt} = -(\Gamma^{-1} - 1)(1 - \lambda)\sigma T_B^2. \quad (\text{B } 1)$$

The final step in deriving equation (4.10) is to use self-similarity to determine,

$$\frac{d \langle \text{TKE}(\text{Ra}_0, \text{Pr}, T_B) \rangle_V}{dt} = \frac{d \langle \text{TKE} \rangle_V}{dT_B} \frac{dT_B}{dt}. \quad (\text{B } 2)$$

Substituting in for Γ and Λ and integrating with respect to T_B , results in

$$\langle \text{TKE} \rangle_V \sim \frac{1}{2}(\Gamma^{-1} - 1)(1 - \Lambda)\text{Ra}_0 \text{Pr} T_B^2, \quad \sigma \gg 1, \quad (\text{B } 3)$$

where Γ is assumed constant and

$$\Lambda = \frac{2}{T_B^2} \int_{T_B} T' \lambda(T') \, dT'. \quad (\text{B } 4)$$

Appendix C. Linear Stability Analysis

The initial evolution of the temperature profiles described in §3 is diffusive. For a deep box, the diffusive temperature solution is

$$\bar{T} = -1 - (1 + T_B) \text{erf}\left(\frac{z}{\delta}\right), \quad \delta = \sqrt{4t}, \quad (\text{C } 1)$$

where T_B is fixed for the purposes of this stability analysis. Here, as we have a deep box, we will redefine $z = 0$ as the top boundary with the domain of interest below. In this analysis, we need to include diffusion of this background profile in the linear stability. We follow the approach of Nijjer et al. (2018) and define the similarity variable

$$\xi = \frac{z}{\sqrt{t}}, \quad (\text{C } 2)$$

such that the background density profile is

$$\bar{T} = -1 - (1 + T_B) \text{erf}\left(\frac{\xi}{2}\right). \quad (\text{C } 3)$$

We want to know the growth rate of infinitesimal modal perturbations to the diffusive background state. The linear vertical velocity (w_ϵ) and temperature (T_ϵ) perturbations are assumed to have the form:

$$\begin{bmatrix} w_\epsilon \\ T_\epsilon \end{bmatrix} = \begin{bmatrix} \hat{w} \\ \hat{T} \end{bmatrix} \tau(t) \exp[i\mathbf{k} \cdot \mathbf{x}]. \quad (\text{C } 4)$$

Following the approach of Drazin and Reid (2004), we linearize the equations of motion (2.4)-(2.6), which will result in a linear eigenvalue problem of the form:

$$\underline{\mathbf{A}} \begin{bmatrix} \hat{w} \\ \hat{T} \end{bmatrix} = \lambda \underline{\mathbf{B}} \begin{bmatrix} \hat{w} \\ \hat{T} \end{bmatrix}, \quad (\text{C5})$$

where $\underline{\mathbf{A}}, \underline{\mathbf{B}}$ are matrix operators and $\lambda = \frac{1}{\tau} \frac{d\tau}{dt} \Big|_{t=t_0}$ is the growth rate of the perturbations at some time t_0 . The solutions to these eigenvalue equations are a function of five parameters: $t_0, k, \text{Ra}, \text{Pr}$, and T_B . We solve these equations using an in-house built eigenvalue solver using Chebyshev differentiation matrices. We found that 50 grid points were sufficient to determine the growth rate of the system. We impose the same top and bottom boundary conditions as in the numerical simulations. Spurious solutions that did not satisfy the appropriate boundary conditions were removed.

Figure 8(a) is a plot of the growth rate (λ) of the linear instability as a function of wavenumber k and t_0 for $\text{Ra} = 10^6, \text{Pr} = 9$, and $T_B = 1$. We first notice that there exists a minimum $t_{0,min}$, below which the system is linearly stable. For $t > t_{0,min}$, the system is unstable for a finite range of wavenumbers and a peak λ at $t \gg t_{0,min}$. Figure 8(b) is a plot of the maximum λ over all wavenumbers, for each time t_0 at different T_B . The maximum λ decreases with T_B until the system becomes stable at finite T_B .

By computing $t_{0,min}$, we determine the earliest time at which the diffusive system becomes linearly unstable. Figure 8(c) is a plot of $t_{0,min}$ as a function of T_B for different Ra . Fitting the data, we find that

$$t_0 = \text{Ra}^{-\frac{2}{3}} \begin{cases} 3T_B^{-1}, & T_B < 0.35 \\ 5T_B^{-\frac{3}{2}}, & T_B \geq 0.35 \end{cases} \quad (\text{C6})$$

This fit is included as dashed/dotted lines in Figure 8(c). As with the nonlinear simulations, we observe that there exists a critical regime change that occurs around $T_B \approx 0.35$. Further, there is a minimum T_B [$T_{B,min}$], where the system is linearly stable for all time and wavenumbers. Figure 8(d) is a plot of the maximum growth rate (λ_{max}) for all k and t_0 as a function of T_B . For T_B close to 1, the growth rate of the system follows

$$\lambda_{max} \approx 0.4\text{Ra}^{\frac{2}{3}}T_B^{\frac{4}{3}} = 0.4\text{Ra}_{eff}^{\frac{1}{3}}. \quad (\text{C7})$$

Again, this fit is included as dashed lines in Figure 8(d). As $T_B \rightarrow T_{B,min}$, λ_{max} diverges from the fit (C7), decreasing rapidly to 0.

For a linear EOS, we know that there is a minimum Rayleigh number below which the system is stable. Similarly, we have found a minimum condition for instability with a quadratic EOS that depends on both Ra and T_B . Figure 8(e) is a plot of $T_{B,min}$ for different values of Ra . Note that this panel has been rotated so that $T_{B,min}$ can be easily compared with panels (c) and (d). We estimate

$$T_{B,min} \approx 0.5\text{Ra}^{-0.45}. \quad (\text{C8})$$

Notice that in terms of Ra_{eff} , this suggests that the convection is stable where $\text{Ra}_{eff} \lesssim \frac{1}{4}$. There exists a minimum stability condition below which the system is linearly stable for these diffusive temperature profiles for all time.

For Ra_{eff} larger than this minimum stability criterion, the analysis highlights that there still

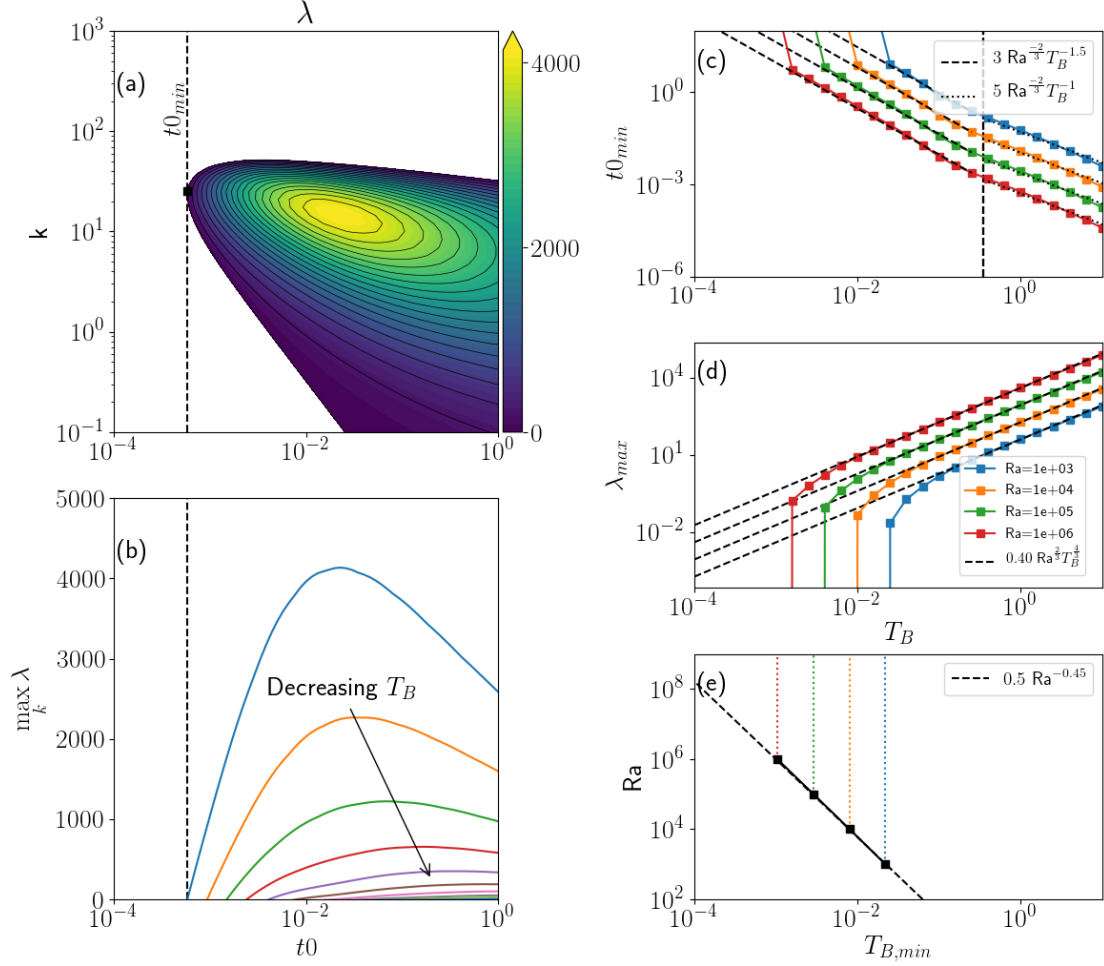


Figure 8: Panel (a) is a contour plot of the growth rate (λ) of the linear instability as a function of t_0 and wavenumber (k). Panel (b) is a plot of the maximum growth rate for all k as a function of t_0 for decreasing T_B . Both panel (a) and (b) are computed for $Ra = 10^6$ and $Pr = 9$. Panel (c) is a plot of the minimum time to instability $t_{0,min}$ below which the system is stable as a function of T_B . We include a vertical line at $T_B = 0.35$ to show a similar regime change to the nonlinear dynamics. Panel (d) is a plot of the maximum growth rate for all k and δ as a function of T_B . Panel (e) is a plot of the minimum T_B below which the system is linearly stable versus Ra .

exists a $t_{0,min}$ (or equivalently a minimum interface thickness), below which the system remains linearly stable. For $t > t_{0,min}$, perturbations about the base state will grow and result in convective mixing of the temperature field. We can compare this minimum time with the numerical simulations.

Figure 9(a) is a plot of the volume integrated turbulent kinetic energy density (TKE). As with the linear stability, the initial temperature stratification is stable, such that TKE initially decays (see Figure 9(a) inset). Once the top boundary layer is sufficiently deep, flow instability results in

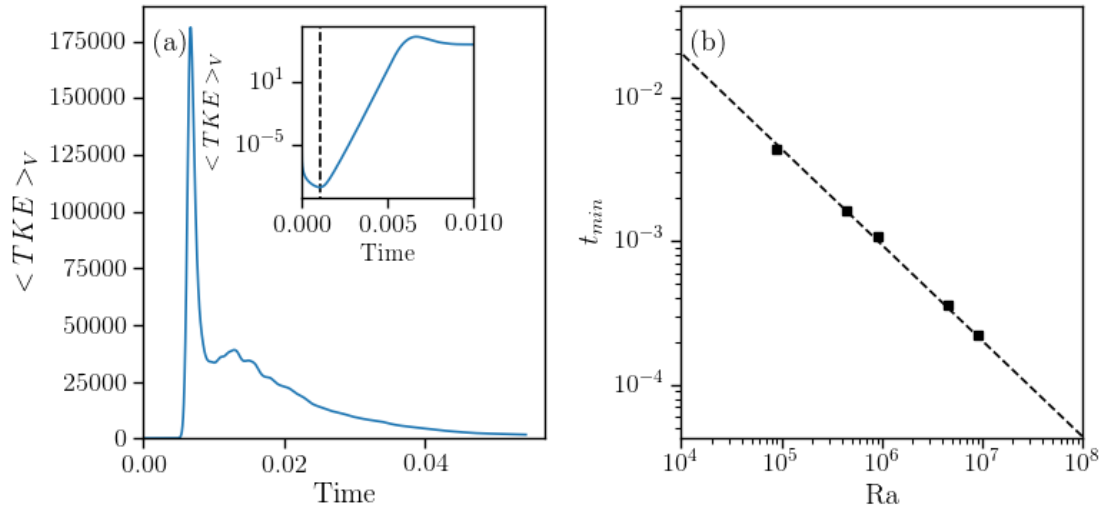


Figure 9: (a) A plot of the kinetic energy as a function of time for Case 3: $Ra_0 = 9.0 \times 10^5$. The inset presents a subset of the data on a log-linear axis to show the initial TKE growth. The vertical dashed line indicates the time of minimum kinetic energy (t_{min}). Panel (b) is a plot of t_{min} as a function of Rayleigh number (Cases 1,2,3,4, and 5). The scaling law (C9) is included as a dashed black line in panel (b).

a large peak in the kinetic energy, which quickly decays back to an equilibrium value. From there, the TKE slowly decays. We define the time when the kinetic energy reaches a minimum (vertical dashed line in Figure 9(a) inset) as t_{min} . Note that this is only an approximation for the time when the system becomes linearly stable. Figure 9(b) is a plot of t_{min} as a function of the Rayleigh number. A fit of the data to the expected power-law suggests that, for the numerical simulations,

$$t_{min} \approx 4.4Ra_0^{-\frac{2}{3}}, \tag{C9}$$

which is close to the expected from linear theory from (C6) with $T_B = 1$.

Appendix D. Resolution and Domain Size Verification

D.1. Domain Dependency

As mentioned in the text, we verified that the present results are not dependent on the box size of the numerical simulations. Figure 10 is similar to Figure 5, with data from two different sized domains. We show that when we double the numerical domain, the temperature decay rate is nearly identical, despite the different initial random noise.

D.2. Resolution Sufficiency

To demonstrate that the numerical simulations are indeed resolved, we have run an additional low-resolution simulation. We re-run Case 3 – $Ra_0 = 9 \times 10^5$, but with a grid resolution of $N_x \times N_y \times N_z = 128 \times 128 \times 128$, or half the resolution in each direction. Figure 11 is a comparison plot

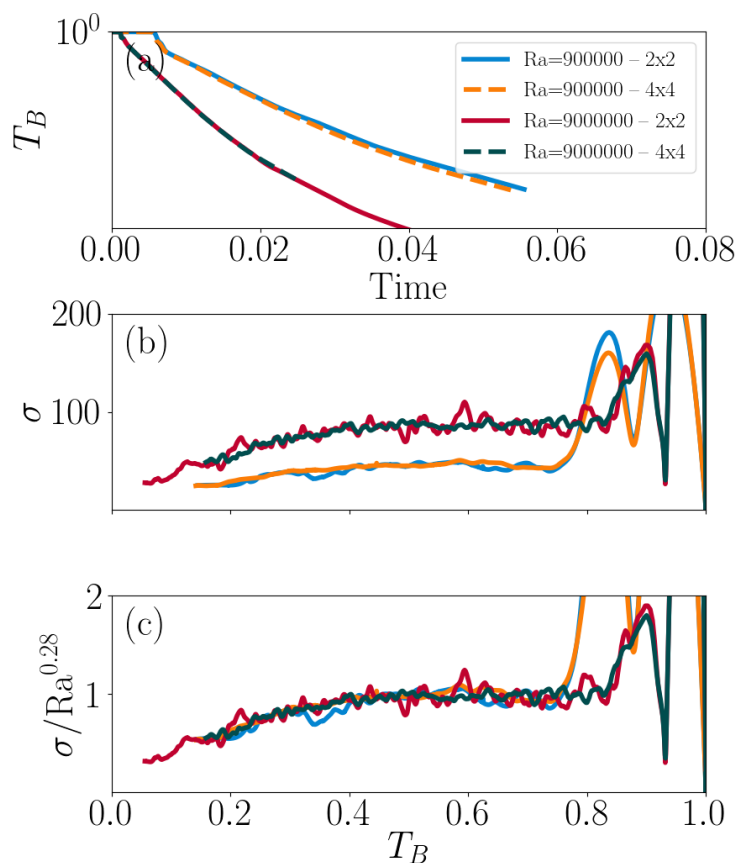


Figure 10: Similar to Figure 5, we demonstrate that the decay rate of change is similar for different sized domains.

between the full-resolution Case 3, and the low-resolution run described here. We observe that the rate of change of temperature is essentially unchanged with one-eighth the number of grid points.

REFERENCES

- Anders, E. H., Vasil, G. M., Brown, B. P., and Korre, L. (2020). Convective dynamics with mixed temperature boundary conditions: Why thermal relaxation matters and how to accelerate it. *Physical Review Fluids*, 5(8).
- Bars, M. L., Lecoanet, D., Perrard, S., Ribeiro, A., Rodet, L., Aurnou, J. M., and Gal, P. L. (2015). Experimental study of internal wave generation by convection in water. *Fluid Dynamics Research*, 47(4):045502.
- Carmack, E. C. (1979). Combined Influence of Inflow and Lake Temperatures on Spring Circulation in a Riverine Lake. *Journal of Physical Oceanography*, 9(2):422–434.
- Chen, C. A. and Millero, F. J. (1986). Thermodynamic properties for natural waters covering only the limnological range. *Limnology and Oceanography*, 31(3):657–662.
- Childs, H., Brugger, E., Whitlock, B., Meredith, J., Ahern, S., Pugmire, D., Biagas, K., Miller, M., Harrison, C., Weber, G. H., Krishnan, H., Fogal, T., Sanderson, A., Garth, C., Bethel, E. W., Camp, D., Rübél,

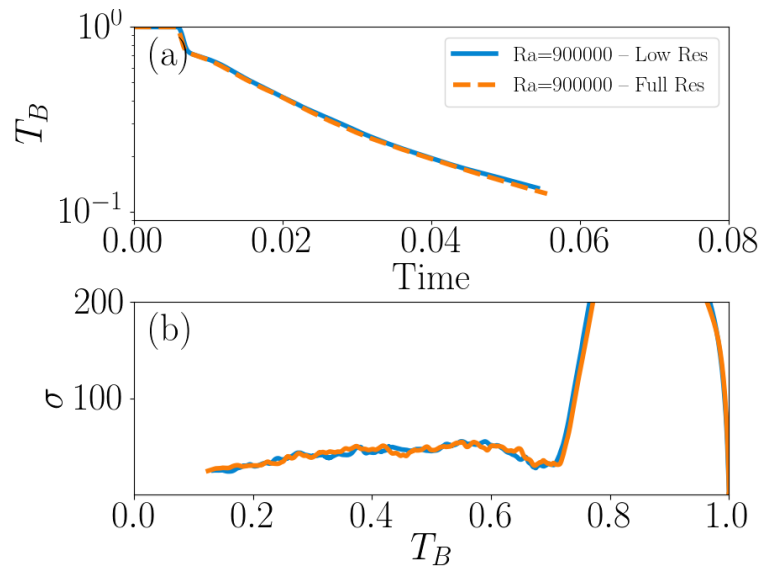


Figure 11: Similar to Figure 5, we demonstrate that the simulation resolution is sufficient to resolve the rate of change of temperature.

- O., Durant, M., Favre, J. M., and Navrátil, P. (2012). VisIt: An End-User Tool For Visualizing and Analyzing Very Large Data. In *High Performance Visualization—Enabling Extreme-Scale Scientific Insight*, pages 357–372.
- Couston, L. A., Lecoanet, D., Favier, B., and Le Bars, M. (2017). Dynamics of mixed convective-stably-stratified fluids. *Physical Review Fluids*.
- Couston, L. A., Lecoanet, D., Favier, B., and Le Bars, M. (2018). The energy flux spectrum of internal waves generated by turbulent convection. *Journal of Fluid Mechanics*.
- Drazin, P. G. and Reid, W. H. (2004). *Hydrodynamic Stability*. Cambridge Mathematical Library. Cambridge University Press, 2 edition.
- Farmer, D. M. (1975). Penetrative convection in the absence of mean shear. *Quarterly Journal of the Royal Meteorological Society*, 101(430):869–891.
- Farmer, D. M. and Carmack, E. (1981). Wind Mixing and Restratification in a Lake near the Temperature of Maximum Density. *Journal of Physical Oceanography*, 11(11):1516–1533.
- Hay, W. A. and Papalexandris, M. V. (2019). Numerical simulations of turbulent thermal convection with a free-slip upper boundary. *Proceedings of the Royal Society A: Mathematical, Physical and Engineering Sciences*, 475(2232):20190601.
- Hewitt, D. R., Neufeld, J. A., and Lister, J. R. (2013). Convective shutdown in a porous medium at high rayleigh number. *Journal of Fluid Mechanics*, 719:551–586.
- Kaminski, A. K. and Smyth, W. D. (2019). Stratified shear instability in a field of pre-existing turbulence. *Journal of Fluid Mechanics*, 862:639–658.
- Kim, J.-H., Moon, W., Wells, A. J., Wilkinson, J. P., Langton, T., Hwang, B., Granskog, M. A., and Rees Jones, D. W. (2018). Salinity control of thermal evolution of late summer melt ponds on arctic sea ice. *Geophysical Research Letters*, 45(16):8304–8313.
- Lecoanet, D., Le Bars, M., Burns, K. J., Vasil, G. M., Brown, B. P., Quataert, E., and Oishi, J. S. (2015). Numerical simulations of internal wave generation by convection in water. *Phys. Rev. E*, 91:063016.
- Nijjer, J. S., Hewitt, D. R., and Neufeld, J. A. (2018). The dynamics of miscible viscous fingering from onset to shutdown. *Journal of Fluid Mechanics*, 837:520–545.

- Olsthoorn, J., Tedford, E. W., and Lawrence, G. A. (2019). Diffused-interface Rayleigh-Taylor instability with a nonlinear equation of state. *Physical Review Fluids*, 4(9):1–23.
- Plumley, M. and Julien, K. (2019). Scaling laws in rayleigh-bénard convection. *Earth and Space Science*, 6(9):1580–1592.
- Smyth, W. D. and Moum, J. N. (2000). Length scales of turbulence in stably stratified mixing layers. *Physics of Fluids*, 12(6):1327–1342.
- Subich, C. J., Lamb, K. G., and Stastna, M. (2013). Simulation of the navier–stokes equations in three dimensions with a spectral collocation method. *International Journal for Numerical Methods in Fluids*, 73(2):103–129.
- Toppaladoddi, S. and Wettlaufer, J. S. (2017). Penetrative Convection at High Rayleigh Numbers. *Physical Review Fluids*, 3(4):43501.
- Townsend, A. A. (1964). Natural convection in water over an ice surface. *Quarterly Journal of the Royal Meteorological Society*, 90(385):248–259.
- Veronis, G. (1963). Penetrative Convection. *Astrogeophys. J.*, 137(641).
- Wang, Q., Zhou, Q., Wan, Z.-H., and Sun, D.-J. (2019). Penetrative turbulent rayleigh-bénard convection in two and three dimensions. *Journal of Fluid Mechanics*, 870:718–734.
- Whipple, G. C. (1898). Classification of Lakes According to Temperature. *Source: The American Naturalist*.